



SDSS-IV MaNGA: The Radial Profile of Enhanced Star Formation in Close Galaxy Pairs

Joshua L. Steffen¹ , Hai Fu^{1,2} , J. M. Comerford³, Y. Sophia Dai (戴昱)⁴ , Shuai Feng^{5,6,7} , Arran C. Gross¹ , and Rui Xue¹

¹ Department of Physics & Astronomy, University of Iowa, Iowa City, IA 52242, USA; joshua-steffen@uiowa.edu

² Institute for Astronomy, University of Hawaii, Honolulu, HI 96822, USA

³ Department of Astrophysical and Planetary Sciences, University of Colorado, Boulder, CO 80309, USA

⁴ Chinese Academy of Sciences South America Center for Astronomy (CASSACA)/National Astronomical Observatories of China (NAOC), 20A Datun Road, Beijing 100012, People's Republic of China

⁵ Department of Physics, Hebei Normal University, 20 South Erhuan Road, Shijiazhuang, 050024, People's Republic of China

⁶ Key Laboratory for Research in Galaxies and Cosmology, Shanghai Astronomical Observatory, Chinese Academy of Sciences, 80 Nandan Road, Shanghai 200030, People's Republic of China

⁷ University of the Chinese Academy of Sciences, No.19A Yuquan Road, Beijing 100049, People's Republic of China

Received 2020 October 26; revised 2021 January 29; accepted 2021 February 1; published 2021 March 11

Abstract

We compare the radial profiles of the specific star formation rate (sSFR) in a sample of 169 star-forming galaxies in close pairs with those of mass-matched control galaxies in the SDSS-IV MaNGA survey. We find that the sSFR is centrally enhanced (within one effective radius) in interacting galaxies by ~ 0.3 dex and that there is a weak sSFR suppression in the outskirts of the galaxies of ~ 0.1 dex. We stack the difference profiles for galaxies in five stellar-mass bins in the range $\log(M/M_\odot) = 9.0\text{--}11.5$ and find that the sSFR enhancement has no dependence on the stellar mass. The same result is obtained when comparison galaxies are matched to each paired galaxy in both stellar mass and redshift. In addition, we find that the sSFR enhancement is elevated in pairs with nearly equal masses and closer projected separations, in agreement with previous work based on single-fiber spectroscopy. We also find that the sSFR offsets in the outskirts of the paired galaxies are dependent on whether the galaxy is the more-massive or less-massive companion in the pair. The more-massive companion experiences zero to a positive sSFR enhancement, while the less-massive companion experiences sSFR suppression in their outskirts. Our results illustrate the complex tidal effects on star formation in closely paired galaxies.

Unified Astronomy Thesaurus concepts: Star formation (1569); Galaxy nuclei (609); Galaxy interactions (600); Galaxy mergers (608); Galaxy pairs (610)

Supporting material: machine-readable table

1. Introduction

In the Λ CDM model, galaxy evolution is a hierarchical process. In this model, massive galaxies are the product of several past merger events of smaller galaxies. In fact, cosmological hydrodynamical simulations have shown that repeated merger events may be responsible for as much as $\sim 60\%$ of the stellar mass in massive galaxies like M87 (e.g., Rodriguez-Gomez et al. 2016; Pillepich et al. 2018). As the galaxies undergo the merging process, the gas within the galaxies is subjected to gravitational torques that perturb the morphology of the galaxies.

The internal dynamics of these interacting galaxies was first modeled in the seminal work by Toomre & Toomre (1972). Since then, hydrodynamical simulations have expanded upon the N -body simulations of Toomre & Toomre (1972) by modeling gas dynamics within the galaxies. These simulations show the process by which barred structures develop within the disks of interacting galaxies due to the tidal torques between them (Barnes & Hernquist 1991). As the bars form, the gases within the galaxy's disk lose angular momentum and get funneled into the centers of the galaxies.

When the gas inflows impact the gases in the nucleus of the galaxy, a burst of new star formation is triggered (Barnes & Hernquist 1996; Mihos & Hernquist 1996). These gas inflows will also bring metal-poor gases from the disk into the center of the galaxy, which can dilute the central metallicity (Rupke et al. 2010; Perez et al. 2011; Scudder et al. 2012). The gas inflows

may also be able to reach into the very center of the galaxy and trigger an episode of supermassive black hole (SMBH) accretion (Capelo et al. 2017).

Interaction-induced star formation was first seen observationally in the bluer colors of peculiar galaxies in Larson & Tinsley (1978). Similar observations have also been shown in more recent works using the single-fiber spectroscopic survey SDSS (Sloan Digital Sky Survey; Ellison et al. 2008; Li et al. 2008; Scudder et al. 2012; Patton et al. 2013; Bustamante et al. 2020). From these previous works, it has been shown that the strength of the star formation enhancement in the centers of paired galaxies is dependent on the stellar mass of the pairs (Li et al. 2008), the projected separation between the pairs (Ellison et al. 2008; Li et al. 2008; Scudder et al. 2012), and the mass ratio between the pairs (Ellison et al. 2008).

The previously mentioned works using SDSS were restricted to studying the centers of the paired galaxies through $1''\text{--}1.5''$ -radius optical fibers. With the recent large integral field spectroscopic (IFS) surveys, interacting galaxies can now be studied with unprecedented spatial detail. These surveys allow us to study the centers of merging galaxies more rigorously since apertures can be set to the physical scale of the galaxies instead of being bound by a fixed sky aperture. These IFS surveys will also allow us to see the extent of the centrally induced star formation and to see how the star formation in the disks of the galaxies is affected.

Indeed, Barrera-Ballesteros et al. (2015) used the CALIFA (Calar Alto Legacy Integral Field Area) survey to study a

sample of 103 paired galaxies by varying the size of the aperture through which the $\text{EW}(\text{H}\alpha)$ is extracted. In this study, they found a moderate enhancement to the specific star formation rate (sSFR) in the centers of paired galaxies and a moderate suppression of the sSFR in the outskirts of the paired galaxies.

Pan et al. (2019) used the SDSS-IV MaNGA survey to study radial profiles of a sample of 205 paired galaxies. The enhancement to the sSFR was shown to be the strongest in the centers of the paired galaxies. This central enhancement linearly fell with increasing galactocentric radii; however, a moderate enhancement to the sSFR remains in the outskirts of the galaxies. Pan et al. (2019) further studied the paired galaxies as a function of merger stage, from well-separated pairs to postmerger galaxies. Across the different merger stages, the sSFR enhancement was greatest in close pairs with tidal features and in postmerger galaxies. This was in agreement with previous hydrodynamical simulations that showed that a burst of star formation is triggered after the first pericenter and as the two galaxies begin to coalesce (Scudder et al. 2012).

The radial profile of sSFR in postmerger galaxies has also been studied with the MaNGA survey by Thorp et al. (2019). The postmerger galaxies were shown to have a strong enhancement to the sSFR in their centers, as well as a moderate enhancement in their outskirts.

Where previous studies on the radial profile of the sSFR offsets in paired galaxies have focused on studying the profiles as a function of interaction stage, we will focus on the radial profile as a function of the stellar mass, projected separation, and mass ratio. As mentioned previously, these parameters have been covered by studies restricted to the nuclear region of the paired galaxies. With the MaNGA survey, we will be able to expand upon these previous studies in greater spatial detail. We will be able to analyze how these three parameters affect both the level of the sSFR offsets in the centers of the paired galaxies and the offsets in the outskirts of the galaxies. We will also be able to study whether any of the three parameters influence the gradient of the sSFR enhancement profiles or if the gradient is preserved between different configurations.

In our previous work using the MaNGA data included in the 14th Public Data Release (DR14; Abolfathi et al. 2018), we built a sample of close galaxy pairs where both components of the pair were contained within the field of view of a single integral field unit (Fu et al. 2018, hereafter Paper I). We found that approximately 5.7% of the MaNGA galaxies have a companion galaxy contained within the field of view of a single integral field unit (IFU). In this work, we update this sample and supplement it with a sample of companion galaxies identified outside the field of view of the MaNGA IFUs.

This paper is organized as follows. In Section 2 we will discuss the properties of the MaNGA survey along with the construction of our pair and control samples. In Section 3 we will discuss how we measure star formation rates and how we build radial profiles of star formation. In Section 4 we study the radial profiles as a function of stellar mass, projected separation, and the mass ratio. In Section 5 we compare our work against previous works, and in Section 6 we summarize the findings of the work. Throughout, we adopt the Λ CDM cosmology with $\Omega_m = 0.3$, $\Omega_\Lambda = 0.7$, and $h = 0.7$.

2. Data and Samples

MaNGA is an IFS survey at the Apache Point Observatory (APO) that uses the SDSS 2.5 m telescope along with two dual-channel BOSS spectrographs (Drory et al. 2015). MaNGA captures spectra through 17 integral field units with variable numbers of fibers: 19, 37, 61, 91, and 127 fibers covering $12''5$, $17''5$, $22''5$, $27''5$, and $32''5$ on the sky, respectively (Law et al. 2015). MaNGA is an optical survey with a spectral coverage of 3600–10300 Å with a resolution of $R \sim 2000$ and a point-spread function (PSF) of $2''5$ FWHM (Bundy et al. 2015).

The MaNGA survey targets galaxies from a subset of 41,154 galaxies in the NASA-Sloan Atlas (NSA v1_0_1; <http://www.nsatlas.org>) with a redshift range of $0.01 < z < 0.15$ and a luminosity range of $-17.7 < \mathcal{M}_i < -24.0$, where \mathcal{M}_i is the rest-frame i -band magnitude within the survey’s elliptical Petrosian apertures. MaNGA plans to cover 10,000 galaxies with a flat stellar-mass distribution at two spatial coverages, $1.5 R_{\text{eff}}$ and $2.5 R_{\text{eff}}$ (where R_{eff} is the radius that contains 50% of the galaxy’s total light). In this work, we use the data from the eighth MaNGA Product Launch (MPL-8), which covers 6142 unique galaxies observed by 2018 July 3.

2.1. Spectral Fitting

We use SPFIT to model the MaNGA data cubes. The IDL package is publicly available⁸ and was first used in our previous study of close galaxy pairs in MaNGA (Paper I). While data products from the MaNGA Data Analysis Pipeline (DAP; Belfiore et al. 2019) and PIPE3D (Sánchez et al. 2016a, 2016b) are available, SPFIT allows us to combine spectra inside a given aperture before fitting the combined spectrum. This feature alone made it better suited for this project. Additional features of SPFIT include (1) simultaneously fitting emission lines and stellar continuum, (2) coadding spaxels with either a Voronoi tessellation or arbitrary polygons while accounting for covariances, (3) modeling asymmetric emission lines, broad active galactic nucleus (AGN) emission lines, AGN continuum, and various dust-extinction laws, and (4) utilizing multithreading when processing a large number of data cubes.

Here we provide a brief description of the fitting procedure of SPFIT. Except for broad-line AGNs, SPFIT models the observed spectrum as a superposition of emission lines and simple stellar populations (SSPs). The SSP library of MUSECAT (Vazdekis et al. 2012) is matched to the MaNGA spectral resolution and is convolved with the line-of-sight velocity distribution (LOSVD). Both the LOSVD and the profile of the emission lines are parameterized as separate Gauss–Hermite series (van der Marel & Franx 1993) to the fourth order.

For model optimization, we prefer a fast algorithm like the Levenberg–Marquardt nonlinear least-squares minimization algorithm implemented in MPFIT (Markwardt 2009). But for complex spectral models like ours, the success of the fitting routine relies on a good initial “guess” solution, which can be provided by the penalized pixel-fitting method (pPXF; Cappellari 2017). The pPXF method is robust because it solves the weights of the templates with a linear algorithm (Lawson & Hanson 1974) *independently* from solving the Gauss–Hermite LOSVD with a nonlinear optimizer (MPFIT). The SPFIT package

⁸ <https://github.com/fuhaiaastro/spfit>

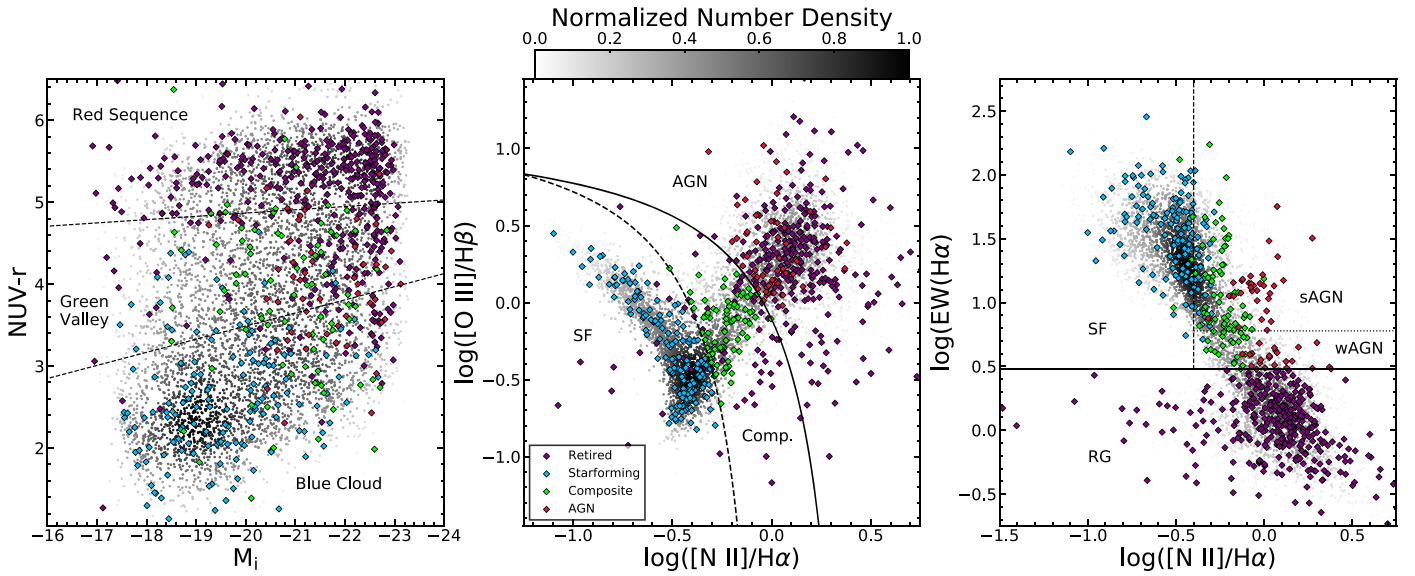


Figure 1. Left: color–magnitude diagram for MaNGA galaxies. Center: BPT (Baldwin, Phillips, and Telervich) diagram for the MaNGA galaxies. Right: the WHAN ($H\alpha$ equivalent width versus $[N II]/H\alpha$) diagram for the MaNGA galaxies. The gray circles represent the whole MaNGA sample, and the color scale reflects the local density around each data point in this color–magnitude plane, as indicated by the color bar on the top. The purple diamonds represent the paired galaxies that are classified as retired (by the $EW(H\alpha)$ cut), the blue diamonds represent the star-forming paired galaxies (by the BPT diagram), the green diamonds represent the composite star-forming-AGN paired galaxies (by the BPT diagram), and the red diamonds represent the paired galaxies containing an AGN (by the BPT diagram).

implements a three-stage fitting procedure. First, it masks out spectral regions around emission lines from the input spectrum and uses pPXF on the masked spectrum with SSP-only templates to obtain the initial “best-fit” parameters of the stellar continuum. Then, it subtracts the best-fit stellar continuum model from the spectrum and uses pPXF to fit the residual emission-line-only spectrum with Gaussian emission-line templates to obtain the initial “best-fit” parameters of the emission lines. Finally, it uses MPFIT on the full input spectrum with the two sets of “best-fit” parameters from pPXF to simultaneously fit all of the parameters describing the emission lines and the stellar continuum. Saved in the final FITS file are the best-fit parameters and their uncertainties, including emission-line fluxes, equivalent widths, and kinematics, and luminosity-weighted stellar masses, ages, metallicities, and kinematics.

2.2. Selecting Star-forming Galaxies

We classify galaxies in this survey as star-forming galaxies by selecting galaxies in the blue cloud on the color–magnitude diagram (CMD). We show the CMD for the MaNGA survey and our pair sample in Figure 1 along with demarcation lines that separate the blue cloud, red sequence, and green valley. We established the demarcation lines by collapsing the CMD to a color histogram for each of the three regions. We then varied the slopes between the regions until we found the slopes that best fit the data. These demarcation lines are

$$NUV - r = 3.1682 - 0.16(\mathcal{M}_i + 18) \quad (1)$$

$$NUV - r = 4.7866 - 0.04(\mathcal{M}_i + 18), \quad (2)$$

where $NUV - r$ is the color from SDSS’s k -corrected absolute magnitude, and \mathcal{M}_i is the i -band magnitude from the NSA catalog.

We use the BPT diagnostic (Baldwin et al. 1981), shown in the center of Figure 1, to remove galaxies with possible AGNs in their centers. Specifically, we use the emission line ratios $\log([O III]/H\beta)$ and $\log([N II]/H\alpha)$, extracted from a 1.3 kpc

aperture, along with the maximum starburst line of Kewley et al. (2001) as the demarcation between the star-forming branch and the AGN branch.

Based on the WHAN diagram, shown in the right panel of Figure 1, we apply an $EW(H\alpha) \geq 6 \text{ \AA}$ cut on galaxy spectra extracted from a $1.0 R_{\text{eff}}$ aperture to ensure that all retired galaxies are removed from the sample (Cid Fernandes et al. 2011).

On top of the star formation cuts, we require that all galaxies are in either the Primary or Secondary MaNGA subsamples (Wake et al. 2017), and that the stellar mass range of the galaxy sample is $\log(M/M_\odot) = 9.0\text{--}11.5$. We use masses calculated from the elliptical Petrosian apertures in the NSA catalog for our total stellar masses.

We build two different pair samples in this work: the inside-IFU sample, which contains paired galaxies where both galaxies are covered by a single MaNGA IFU, and the outside-IFU sample, where a MaNGA target galaxy is coupled with another galaxy found outside of its MaNGA IFU.

2.3. Inside-IFU Sample

To identify potential paired galaxies covered by individual IFUs, we start by overlaying SDSS photometric objects on each MaNGA field of view. We manually inspect each MaNGA field, removing photometric objects that are over-deblended galaxy fragments and, very rarely, adding any objects missed in the SDSS photometric catalog. At this stage, the object catalog includes foreground stars and foreground/background galaxies along with the potential paired galaxies.

To select paired galaxies from our object catalog, we inspect the spectra of each object. The spectra of the identified objects are extracted through a $1''$ circular aperture and fitted assuming the MaNGA target’s redshift and then manually sorted into the following categories: “good” galaxy spectra, broad-line AGNs, foreground star, foreground/background galaxies, or objects with poor signal-to-noise ratio (S/N). The “good” galaxy spectra are the objects whose spectra are well modeled by SPFIT

Table 1
Close Galaxy Pairs and Multiples in MaNGA IFUs

Plate-IFU	Index	R.A. (J2000) (deg)	Decl. (J2000) (deg)	Redshift
7443-12703	0	229.5255758	+42.7458538	0.04043
...	1	229.5265348	+42.7440666	0.04079
7958-3701	0	257.5338400	+33.5989046	0.11015
...	1	257.5344200	+33.5984600	0.10920
...	2	257.5326566	+33.5979470	0.11031
7960-3701	0	257.0857469	+31.7469109	0.10819
...	1	257.0850100	+31.7470300	0.10800
7960-3702	0	258.2893316	+31.5820375	0.02961
...	1	258.2913540	+31.5812244	0.02943
7962-3702	0	259.0637432	+28.0140065	0.10725
...	1	259.0639447	+28.0130439	0.10753

Note. This table lists a total of 404 plate-IFUs that contain close galaxy pairs and multiples in the eighth MaNGA Product Launch (MPL-8). The second column lists the component index, where “0” indicates the primary target of the MaNGA observation. For each IFU, all components within $\pm 2000 \text{ km s}^{-1}$ of the primary are listed, sorted in ascending angular distance from the primary. (This table is available in its entirety in a machine-readable form in the online journal. A portion is shown here for guidance regarding its form and content.) (This table is available in its entirety in machine-readable form.)

at the target galaxy’s redshift, whether it is the target galaxy itself or a nearby companion galaxy. This means that the companion galaxy can be within approximately $\pm 2000 \text{ km s}^{-1}$ of the MaNGA target. We found 6573 “good” objects, 57 broad-line AGNs, 836 foreground stars, 319 foreground/background galaxies, and 1546 objects with poor S/N.

Broad-line AGNs comprise $\sim 0.9\%$ of MaNGA’s galaxy sample, whereas Lacerda et al. (2020) found $\sim 2.8\%$ from the CALIFA survey and Sánchez et al. (2018) found $\sim 1.33\%$ from the MaNGA’s MPL-5 sample (which observed ~ 2700 galaxies).

Among the 6142 MaNGA IFUs considered here, 404 cover close galaxy pairs and multiples. The sample includes 327 pairs, 67 triplets, seven quadruplets, and one quintuplet. Table 1 lists the coordinates and redshifts of these galaxy components in pairs/multiples. When a MaNGA target has multiple companion galaxies, we chose the closest companion to define the pair’s mass ratio and projected separation.

For this study, we further restrict the sample by setting a relative velocity cut of $\Delta v < 500 \text{ km s}^{-1}$. Given the redshift range of the MaNGA sample and the size of MaNGA’s IFUs, the maximum projected separation for a companion galaxy in the IFU is $\sim 40 \text{ kpc}$. Again, the galaxy sample is also restricted to galaxies with a stellar mass range of $\log(M/M_\odot) = 9.0\text{--}11.5$ and galaxies in the Primary or Secondary MaNGA subsamples. We also require that the galaxies are classified as star-forming as described in Section 2. These requirements reduce our sample down to 54 star-forming MaNGA targets with inside-IFU companions. While we use the identified companions to select galaxy pairs, we only build radial profiles for the MaNGA target galaxies. We do this because the identified companions are not included in the NSA catalog that we use to build the radial profiles for the galaxies.

2.4. Outside-IFU Sample

We supplement the inside-IFU sample with a set of pairs identified outside of the field of view of the MaNGA IFU. We select these outside-IFU pairs from the NSA catalog. We search

for these external pairs by selecting objects with a projected separation from the MaNGA targets of $r_p < 50 \text{ kpc}$ using the MaNGA target’s redshift. We further use a relative velocity cut of $\Delta v < 500 \text{ km s}^{-1}$ to remove projected galaxies from the selection.

From the NSA catalog’s 641,409 galaxies, we find 492 galaxies that are paired to MaNGA targets. After restricting the sample to SFGs, we have another 115 MaNGA targets with paired galaxies outside of the IFU. MaNGA targets that have both an inside-IFU and an outside-IFU pair are left to the inside-IFU sample.

2.5. Control Sample

To show how the population of galaxy pairs differs from isolated galaxies, we will compare our pair sample to a sample of control galaxies in the MaNGA survey. We build this control sample from the MaNGA target galaxies that have no spectroscopic companions within $r_p < 50 \text{ kpc}$ and $\Delta v < 500 \text{ km s}^{-1}$ either inside or outside of the IFU. This gives us a control sample of 1830 star-forming control galaxies.

It has been shown that the SFR in galaxies is dependent on both the stellar mass and the redshift of the galaxies (e.g., Noeske et al. 2007). We will compare our interacting galaxies with control galaxies of a similar stellar mass, redshift, and radial size to account for these other dependencies. To do this, we will use two different methods of pair-control comparison.

In the first method, we simply control for the stellar mass between the pairs and controls. We split both the pair and control samples into five evenly spaced stellar-mass bins over the range $\log(M/M_\odot) = 9.0\text{--}11.5$. The pairs are then compared to their respective controls within each stellar-mass bin. While the redshift is not constrained in this method, we will show in Section 4.1.1 that this method is sufficient to reveal the merger-induced star formation.

In the second method, we select a “tailored” control sample for each paired galaxy from the full sample of isolated galaxies. We select a subsample of 20 control galaxies for each paired galaxy. We first select all of the control galaxies that are within 0.1 dex in stellar mass, 0.025 in redshift, 20% in effective radii, and within the same MaNGA subsample (e.g., Primary or Secondary) as the paired galaxy. With these requirements, most paired galaxies will find between 20 and 60 control galaxies. Since we want each paired galaxy to be treated in a similar manner, we randomly downselect the total number of acquired control galaxies to 20. A given control galaxy may be selected for multiple pairs by the pipeline; most of the control galaxies are used at least once, and the average number of times a given control is reused is between two and four times. In the cases where a paired galaxy does not initially acquire 20 control galaxies, we iteratively expand the stellar mass limit by 0.1 dex, the redshift by 0.025, and the R_{eff} by 5% until at least 20 control galaxies are found. We found that 39 pairs required one extra iteration, 15 pairs required two extra iterations, five pairs required three extra iterations, and two pairs required four extra iterations.

3. Analysis Methods

3.1. Specific Star Formation Rate

We calculate the star formation rates in the pair and control galaxies with the emission lines extracted with our spectra fitting code, SPFIT (described in Section 2.1). We correct the emission

lines for reddening using the extinction curve from Cardelli et al. (1989) with updated coefficients from O'Donnell (1994). The extinction is parameterized as $R_V \equiv A_V/E(B-V) = 3.1$, where we estimate the value of the V -band extinction, A_V , by comparing the $H\alpha/H\beta$ ratio to the expected value of 2.85 for Case B recombination.

We measure the SFR from the extinction-corrected $H\alpha$ luminosity, $L_{H\alpha}$. We use the SFR formula, Equation (3), from Murphy et al. (2011), which uses a Kroupa initial mass function (IMF), solar metallicity, a constant SFR at an age of 100 Myr, and Case B recombination:

$$\frac{\text{SFR}}{M_\odot \text{ yr}^{-1}} = \frac{L_{H\alpha}}{1.86 \times 10^{41} \text{ erg s}^{-1}}. \quad (3)$$

Since the stellar mass of a galaxy is not uniformly distributed within the galaxy, we normalize the SFR by the stellar mass in the same spaxel, M , giving us the specific star formation rate:

$$\text{sSFR} = \frac{\text{SFR}}{M}. \quad (4)$$

The local stellar masses used here are derived from SPFIT's best-fit stellar continuum. Utilizing sSFR instead of SFR allows us to compare regions of high mass surface density to regions of low mass surface density.

We check our measurement of the specific star formation rate with the equivalent width of the $H\alpha$ line, $\text{EW}(H\alpha)$, since it is a known proxy for the sSFR. This is useful as the sSFR is dependent on SPFIT's measurement of the stellar mass while $\text{EW}(H\alpha)$ is an observable. As we will show in Section 4, the radial profiles of $\text{EW}(H\alpha)$ are consistent with the radial profiles of the sSFR.

The S/N of the data will decrease with wide galactocentric radii. MaNGA is designed to cover $1.5 R_{\text{eff}}$ for galaxies in the Primary sample and $2.5 R_{\text{eff}}$ in the Secondary sample. These are not hard limits, and data will exist beyond these radii, especially along the semiminor axis of galaxy; however, the data beyond these limits may be unreliable due to low S/N. To control the quality of the data used, we only use spaxels with $\text{S/N} \geq 3$ for the $H\alpha$ line. We also restrict the spaxels used to those with $\text{EW}(H\alpha) \geq 6 \text{ \AA}$ to remove retired regions from the survey (Cid Fernandes et al. 2011), which effectively sets -10.8 yr^{-1} as the lower limit to the sSFR in our galaxies.

3.2. Radial Profiles

In order to spatially characterize the star formation in the paired galaxies, we build radial profiles of sSFR. First, the geometry of the galaxies needs to be defined. Specifically, we will need the position angle, the inclination angle, and the effective radius of each of the MaNGA targets. We use the r -band elliptical Petrosian apertures from the NSA catalog and the r -band Sérsic apertures from Simard et al. (2011) to define the geometries of the galaxies.

The NSA catalog has complete coverage over the MaNGA sample (since MaNGA selects its targets from this catalog); however, it tends to fail to properly fit paired galaxies with close on-sky separations. We found that the apertures from Simard et al. (2011) work better for these close paired galaxies; however, the catalog does not completely cover the MaNGA sample. We use the NSA catalog for the outside-IFU pair sample because they are well separated on the sky. The Simard et al. (2011) catalog is used for the inside-IFU sample. If the

paired galaxy is not covered by Simard et al. (2011), we use the ellipse from the NSA catalog.

We fit the geometry with apertures from both catalogs when available. When using the first method of pair-control comparison, where pairs and controls are grouped into stellar mass bins, we fit the control galaxies with the NSA apertures. When making the comparison with the second method, paired galaxies fitted with the NSA apertures are compared against controls fitted with the NSA apertures, and paired galaxies fitted with the Simard et al. (2011) apertures are compared against controls fitted with the Simard et al. (2011) apertures. Further, when defining a galaxy's geometry with the Simard et al. (2011) apertures, we also use the masses given in the catalog for the total stellar mass of the galaxy. Note that although we carefully treat the two catalogs separately whenever possible, we find excellent agreement in the geometry parameters of the control galaxies in both catalogs.

We calculate the inclination angle, i , of the galaxies using the major-to-minor axis ratios from the elliptical apertures:

$$\cos^2(i) = \frac{(b/a)^2 - q^2}{1 - q^2}, \quad (5)$$

where b/a is the major-to-minor axis ratio and q is the intrinsic oblateness. We use the empirically determined oblateness of $q = 0.13$ from Giovanelli et al. (1994).

The inclination angle, along with the galaxy's position angle, is used to deproject the geometries of the galaxies. We use the 50% half-light radius (i.e., the effective radius, R_{eff}) to scale the sizes of the galaxies. Doing this will allow us to compare galaxies of different sizes against each other.

Once the geometries of the galaxies are set, we can build azimuthally averaged radial profiles. The spaxels are binned into radius increments of $0.2 R_{\text{eff}}$ from 0.0 to $2.6 R_{\text{eff}}$. Within each radius bin, we take the median of the specific star formation rate. We build an azimuthally averaged radial profile for each MaNGA star-forming galaxy and later stack and differentiate these profiles in the subsequent analysis.

The MaNGA sample does not have a uniform spatial coverage; 63% of the sample is designed to cover $1.5 R_{\text{eff}}$ (the Primary+ subsample), and 37% of the sample is designed to cover $2.5 R_{\text{eff}}$ (the Secondary subsample). This means that there will be fewer selected spaxels beyond $1.5 R_{\text{eff}}$ and the S/N of the selected spaxels will be lower than those within $1.5 R_{\text{eff}}$. We decide to still extend our radial profiles out to $2.5 R_{\text{eff}}$ to make full use of the MaNGA data; however, we emphasize that the difference in the sampling of the data within $1.5 R_{\text{eff}}$ and the data beyond $1.5 R_{\text{eff}}$ may create artificial slopes in the data.

4. Results

4.1. Star Formation Enhancement

With the individual $\log(\text{sSFR})$ profiles built for each MaNGA galaxy, we now use two different methods to compare the profiles of paired galaxies against the profiles of control galaxies. In the first method, in Section 4.1.1, paired galaxies are compared to control galaxies within evenly spaced stellar-mass bins. In the second method, in Section 4.1.2, paired galaxies are compared to a subset of 20 control galaxies that are matched in stellar mass and redshift.

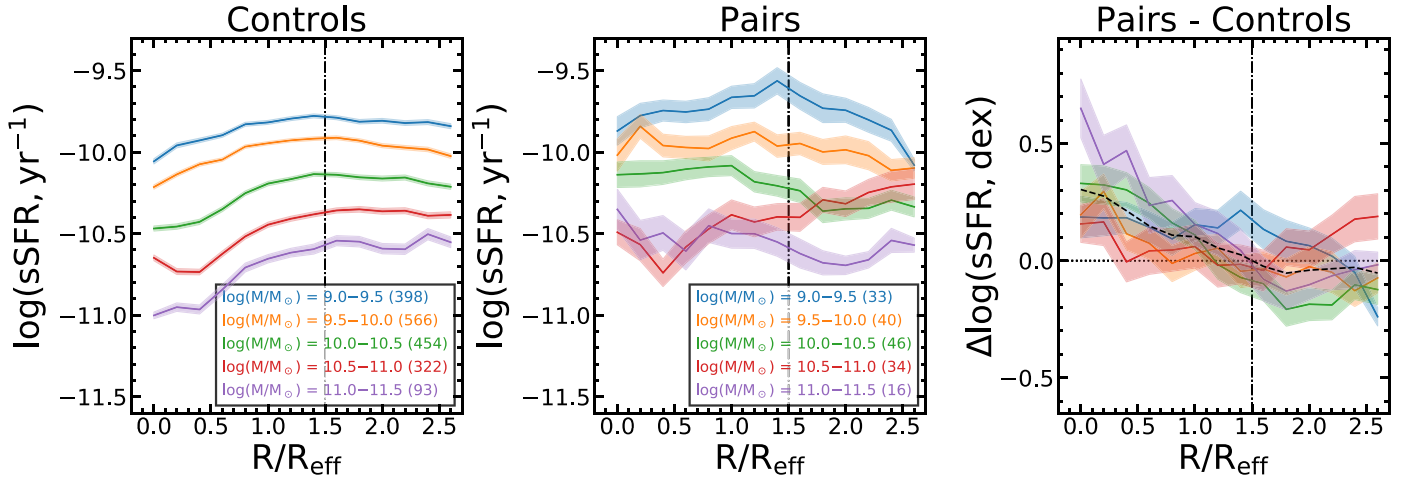


Figure 2. The $\log(\text{sSFR})$ as a function of galactocentric radius for control galaxies (left) and galaxy pairs (middle). The differences between the profiles of the paired galaxies and the control galaxies are shown in the right panel. The dashed black profile represents the mean of the difference profiles. The colors of the profiles represent the mass range of the selected galaxies, which are given in the legend along with the number of galaxies in that mass bin in parentheses. The highlighted region around the profiles represents the standard error of the mean of the data at the given radius interval. The vertical dashed-dotted line marks $1.5 R_{\text{eff}}$, beyond which the radial sampling is expected to fall.

4.1.1. Mass-binned Difference Profiles

In the first method, paired and control galaxies are grouped into five evenly spaced stellar-mass bins in the range $\log(M/M_{\odot}) = 9.0-11.5$. Within each stellar-mass bin, we create a median profile of $\log(\text{sSFR})$ as a function of R_{eff} -scaled galactocentric distance for both paired and control galaxies. The control profiles are constructed using all available control galaxies within each mass bin. The error associated with the “stacked” profile is the standard error of the mean of the data at each radius bin. Here we define the standard error of the mean, $\sigma_{\bar{x}}$, as

$$\sigma_{\bar{x}} = \frac{\sigma}{\sqrt{n}}, \quad (6)$$

where σ is the standard deviation and n is the sample size.

We show these stacked profiles for control galaxies in the left-hand panel of Figure 2 and the stacked profiles for paired galaxies in the middle panel of Figure 2. Star formation in the control galaxies is quenched in their centers with respect to their disks, and the difference between the sSFRs in their centers and their disks increases with stellar mass, consistent with previously published results using the MaNGA survey (Belfiore et al. 2018). In contrast, the paired galaxies show flatter sSFR profiles, where the level of the sSFR remains roughly consistent across their disks, except for paired galaxies with stellar masses above $\log(M/M_{\odot}) = 10.5$, which still show some central quenching.

We then take the differences between the stacked profiles of the paired galaxies and the control galaxies, pair minus control, in log space (this means that the difference profiles really represent a ratio between the pairs and controls in linear space). This gives us the difference profile, $\Delta \log(\text{sSFR})$, which shows us where the sSFR is enhanced or suppressed (shown in the right-hand panel of Figure 2). Across all stellar mass bins, the sSFRs of paired galaxies are centrally enhanced by $\sim 0.3 \pm 0.1$ dex, which gradually falls to zero around $\sim 1.5 R_{\text{eff}}$. In the outskirts of the pairs beyond $1.5 R_{\text{eff}}$, the pairs feature lightly suppressed sSFRs of 0.0–0.1 dex. All of the mass ranges except for the highest mass range, $\log(M/M_{\odot}) = 11.0-11.5$, trend close to the median profile. For the most massive galaxies,

$\log(M/M_{\odot}) = 11.0-11.5$, the enhancement to the sSFR within $0.5 R_{\text{eff}}$ is significantly higher than the median profile (reaching 0.5–0.6 dex). As will be discussed in Section 4.1.2, we believe this elevated enhancement in the highest mass bin is driven by more compact mergers instead of stellar mass.

In summary, Figure 2 shows that the merger process is capable of rejuvenating star formation in the centers of these galaxies, resulting in almost flat sSFR radial profiles. In addition, the sSFR enhancement is mass independent: star formation proceeds at $\sim 2\times$ (0.3 dex) greater rates in galaxies with close companions than in more isolated galaxies, across a wide mass range of $9.0 \leq \log(M/M_{\odot}) \leq 11.5$.

We repeat this analysis for the EW($H\alpha$) in Figure 3. We find that the EW($H\alpha$) profiles are in close agreement with the sSFR profiles, which shows that we can be confident of SPFIT’s measurement of the sSFR. We do see that the pair–control offsets are lightly suppressed using the EW($H\alpha$), as the $\Delta \log(\text{EW}(H\alpha))$ is only enhanced by 0.25 dex where the $\Delta \log(\text{sSFR})$ was enhanced by 0.30 dex.

This method of stacking sSFR profiles by a single parameter (stellar mass) has the advantage of simplicity and large statistical samples. It has revealed the first-order result of mass-independent, centrally enhanced star formation in close galaxy pairs. To proceed with exploring the dependency of ΔsSFR on merger parameters such as separation and mass ratio, we will utilize a more sophisticated method of selecting control samples for individual paired galaxies based on stellar mass and redshift in the following subsections.

4.1.2. Tailored-control Difference Profiles

In the second method, we match each paired galaxy to a set of 20 control galaxies of similar stellar masses and redshifts, as described in Section 2.5. We then take the median of the azimuthally averaged profiles of the tailored-control sample. Finally, we obtain the $\Delta \log \text{sSFR}$ profile for each of the 169 paired galaxies by calculating the difference between its sSFR profile and the median profile of its control sample.

Before delving into merger parameters, we decided to stack the profiles by stellar mass to see how this method compares to the previous mass-binning method. We split the individual

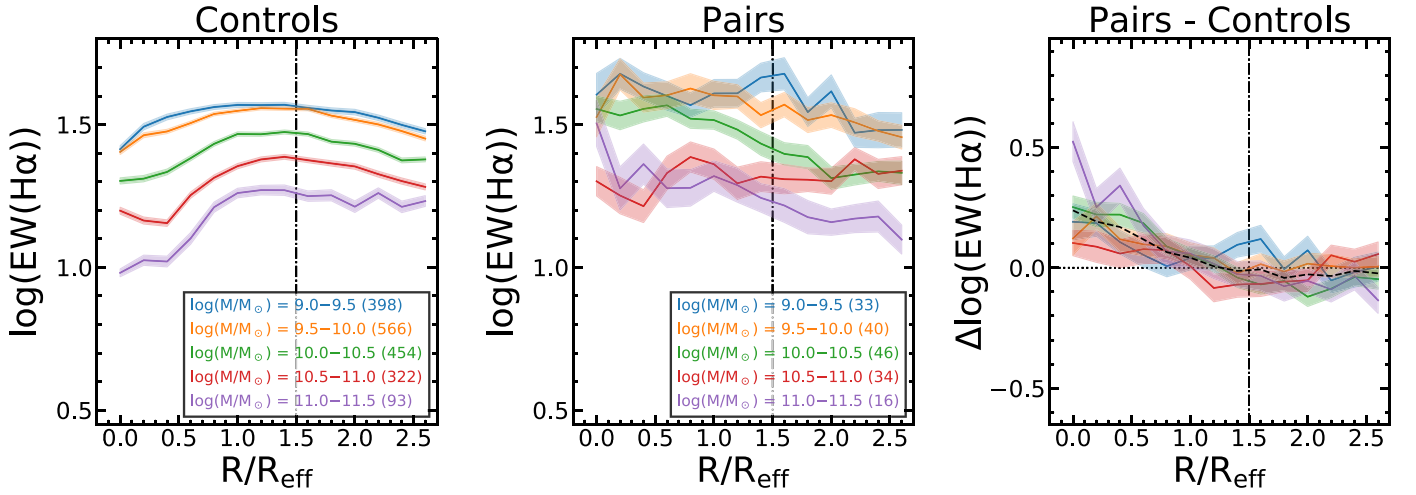
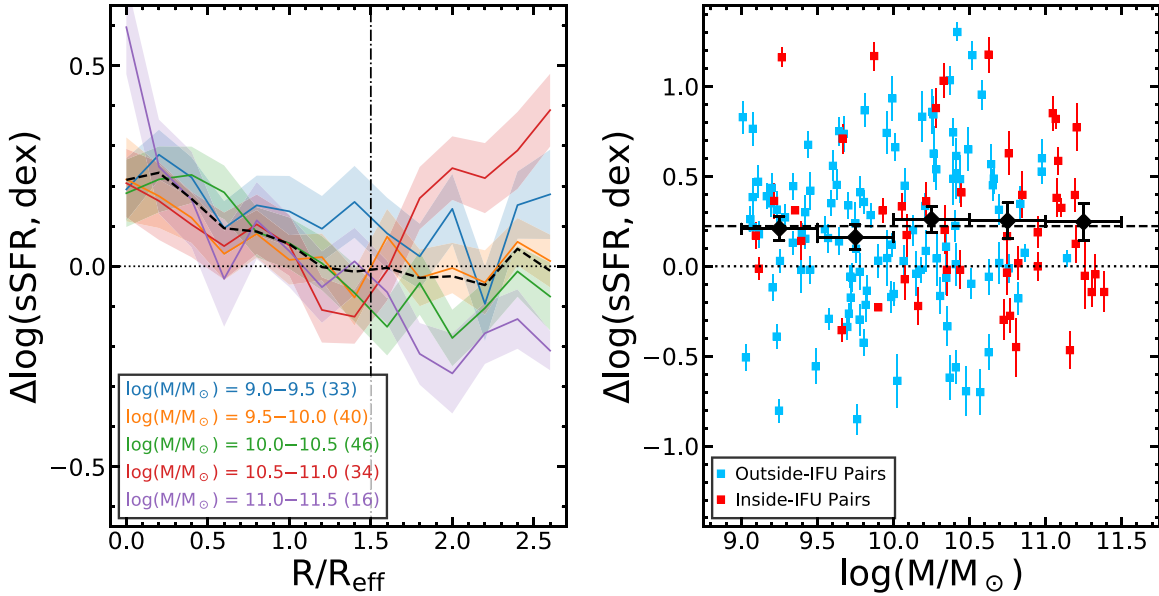
Figure 3. Same as Figure 2 but for EW(H α).

Figure 4. The left panel shows the $\Delta\log(\text{sSFR})$ profiles where the difference profiles are constructed from the difference between the paired galaxy profiles and a set of 20 control galaxies. The profiles are split into five different stellar-mass bins, and the highlighted regions around the profiles represent the standard error of the mean of the profile. The black dashed line represents the mean profile between the four difference mass ranges. The number of paired galaxies in each mass range is given in the legend in parentheses. The right panel shows the nuclear $\Delta\log(\text{sSFR})$ extracted from a $0.5 R_{\text{eff}}$ aperture. The black squares are the mean values within a stellar-mass bin (where the sizes of the bins are shown with the horizontal error bars). The vertical error bars represent the standard deviation within the bin. The horizontal, dashed black line represents the median central enhancement of the pair sample. Galaxies in the outside-IFU (blue) and inside-IFU (red) samples are separately depicted. The vertical dashed-dotted line marks $1.5 R_{\text{eff}}$, beyond which the radial sampling is expected to fall.

difference profiles into five evenly spaced stellar-mass bins in the range $\log(M/M_{\odot}) = 9.0\text{--}11.5$ and stack the difference profiles within each mass bin. This gives us five difference profiles covering five different stellar-mass ranges shown in the left-hand panel of Figure 4. The errors of the stacked profiles are the standard error of the mean of the difference profiles within each bin.

To focus on the sSFR offsets in the centers of the galaxies, we also calculate the sSFR difference between each paired galaxy and its control sample within the central $0.5 R_{\text{eff}}$. The central sSFR is calculated for each galaxy by taking spaxels within $0.5 R_{\text{eff}}$ and whose H α flux has $S/N \geq 3$ and then taking the median value of sSFR of the selected spaxels. Once this is done, we calculate the $\Delta\log(\text{sSFR})$ using the same method as was used for the $\Delta\log(\text{sSFR})$ radial profiles. The central sSFR

of a paired galaxy is compared against the sSFR of a set of 20 similar control galaxies, the same set of controls that were used for the $\Delta\log(\text{sSFR})$ profiles, by taking the difference between the central sSFR of the paired galaxy and the median sSFR of the 20 selected control galaxies. We depict the central $\Delta\log(\text{sSFR})$ as a function of stellar mass in the right-hand panel of Figure 4.

The difference profiles are shown to be centrally enhanced by $\sim 0.20\text{--}0.25 \pm 0.1$ dex. Similar to what was seen in Section 4.1.1, the level of the enhancement is independent of galaxy mass with the exception of the highest mass bin, $\log(M/M_{\odot}) = 11.0\text{--}11.5$, which is 0.4 dex higher than the sample average.

The central enhancement to the sSFR falls to zero around $1.2 R_{\text{eff}}$, and the outskirts of the galaxies are lightly suppressed by

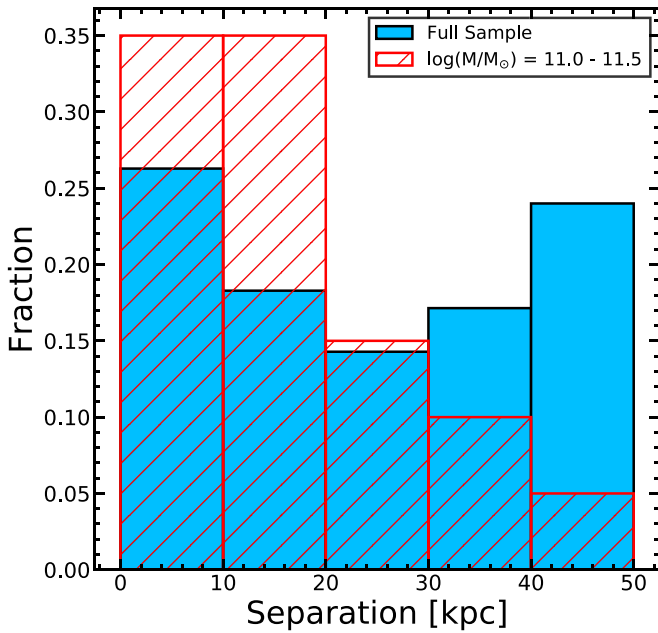


Figure 5. Projected separation distribution of the whole sample (blue) against the projected separation distribution for the highest mass galaxies, $\log(M/M_{\odot}) = 11.0 - 11.5$ (red).

0.0–0.1 dex. Within individual mass ranges, there are some mass ranges that feature large enhancements to the sSFR at large radii, while other mass ranges show a strong suppression of the sSFR. There appears to be no dependence on the stellar mass of the pair, but, as we will show in Section 4.2, these offsets at large radii may be dependent on the mass ratio between the galaxy pairs.

To understand why the profiles of high-mass galaxies behave differently from the rest of the sample in Figures 2, 3, and 4, we compare the distribution of the projected separation for the whole sample and for galaxies in the highest mass bin in Figure 5. The whole sample has a V-shaped separation distribution. This is the result of the combination of the two different samples, the inside-IFU and outside-IFU samples. The outside-IFU sample should find more pairs at wide projected separations due to the larger volume to find companions in. The separation distribution of the inside-IFU sample is limited by MaNGA’s IFU sizes and the sample’s redshift distribution; the maximum possible projected separation for a MaNGA target with $z = 0.15$ and a 127 spaxel IFU is about 40 kpc.

The highest mass galaxies in the sample are at closer projected separations in comparison to the rest of the sample, with 70% of the highest mass galaxies being within 20 kpc. The cause of this may be clustering effects where high-mass galaxies tend to be at the centers of galaxy clusters (Cooray & Sheth 2002; Zehavi et al. 2002). As we will show in Section 4.3, the central sSFR enhancement is strongest at small projected separation, which means that higher sSFRs in the centers of the massive galaxies may be driven by their close projected separations.

The results we obtain from the tailored-control method is largely consistent with the mass-binning method. Between the two methods, we see that the $\Delta\log(\text{sSFR})$ profile is independent of the total stellar mass of the galaxies. In the next two sections, we will use the tailored-control method to study how the difference profiles behave as a function of the mass ratio (Section 4.2) and projected separation (Section 4.3).

4.2. Dependence on Mass Ratio

While the centrally enhanced star formation in close galaxy pairs seems mostly mass independent, the mass ratio of the galaxy pair, like the projected separation, may be an important parameter that controls the level of enhancement (Ellison et al. 2008).

The mass ratio here is defined as

$$\Delta\log(M) = \log(M_{\text{target}}) - \log(M_{\text{comp}}), \quad (7)$$

where M_{target} is the stellar mass of the MaNGA target galaxy, and M_{comp} is the stellar mass of its identified companion galaxy. In the inside-IFU sample, we have stellar masses for the MaNGA target galaxy but not the other identified pairs. Because of this, we leave the inside-IFU companions out of this analysis.

In the top left of Figure 6, we split the $\Delta\log(\text{sSFR})$ profiles into four mass ratio bins in $|\Delta\log(M)| = 0.0 - 1.0$. Here, $|\Delta\log(M)| \leq 0.5$ represents equal-mass major mergers, while $|\Delta\log(M)| \geq 0.5$ represents minor mergers. We see that there is a clear preference for pairs in major mergers to have higher sSFR enhancements in their centers, $\sim 0.3 - 0.4$ dex, while minor mergers show a weaker sSFR enhancement of $\sim 0.0 - 0.2$ dex. The effect can be seen more clearly with the data extracted from the central $0.5 R_{\text{eff}}$ in the top right panel. Here the $\Delta\log(\text{sSFR})$ falls linearly with wider mass ratios, reaching zero enhancement to the sSFR at $|\Delta\log(M)| = 1.5 - 1.75$.

We use the mass ratio not only to study how a major merger behaves differently from a minor merger but also to study how the more-massive galaxy of a pair behaves differently from the less-massive galaxy of the pair. We expect that either component of a similar-mass pair will behave in a similar fashion; however, in a minor merger, the large central galaxy may not respond to the merger event in the same way as its less-massive companion. The two different scenarios can be differentiated with our definition of the mass ratio in Equation (7): when the MaNGA target is the more-massive companion of the pair, its mass ratio is positive, and when the MaNGA target is the less-massive companion of pair, the mass ratio is negative. To distinguish between these scenarios, we refer to the more-massive galaxy of a pair as the primary companion and the less-massive galaxy of a pair as the secondary companion.

In bottom left panel of Figure 6, we split the profiles by mass ratio into four bins. The primary companions are the pairs with $\Delta\log(M) \geq 0.0$, and the secondary companions are the pairs with $\Delta\log(M) \leq 0.0$. When splitting the mass ratio like this, we see that major mergers have still higher levels of sSFR enhancement than minor mergers do; however, we also see that the less-massive companion of the pair sees a higher $\Delta\log(\text{sSFR})$ than the more-massive companion of a pair. In major mergers, the sSFR enhancement is ~ 0.1 dex higher in secondary companions than in primary companions. In minor mergers, the sSFR enhancement is ~ 0.2 dex higher in secondary companions than in primary companions.

In bottom right panel of Figure 6, we see that the sSFR enhancement is strongest in galaxies close to a 1:1 mass ratio ($\Delta\log(M) = 0.0$). These galaxies feature a central enhancement of ~ 0.4 dex, which is 0.2 dex higher than the average central enhancement of the whole sample. This enhancement falls within wider mass ratios with a different slope for primary and secondary companions. At $\Delta\log(M) = -1.0$, the sSFR is

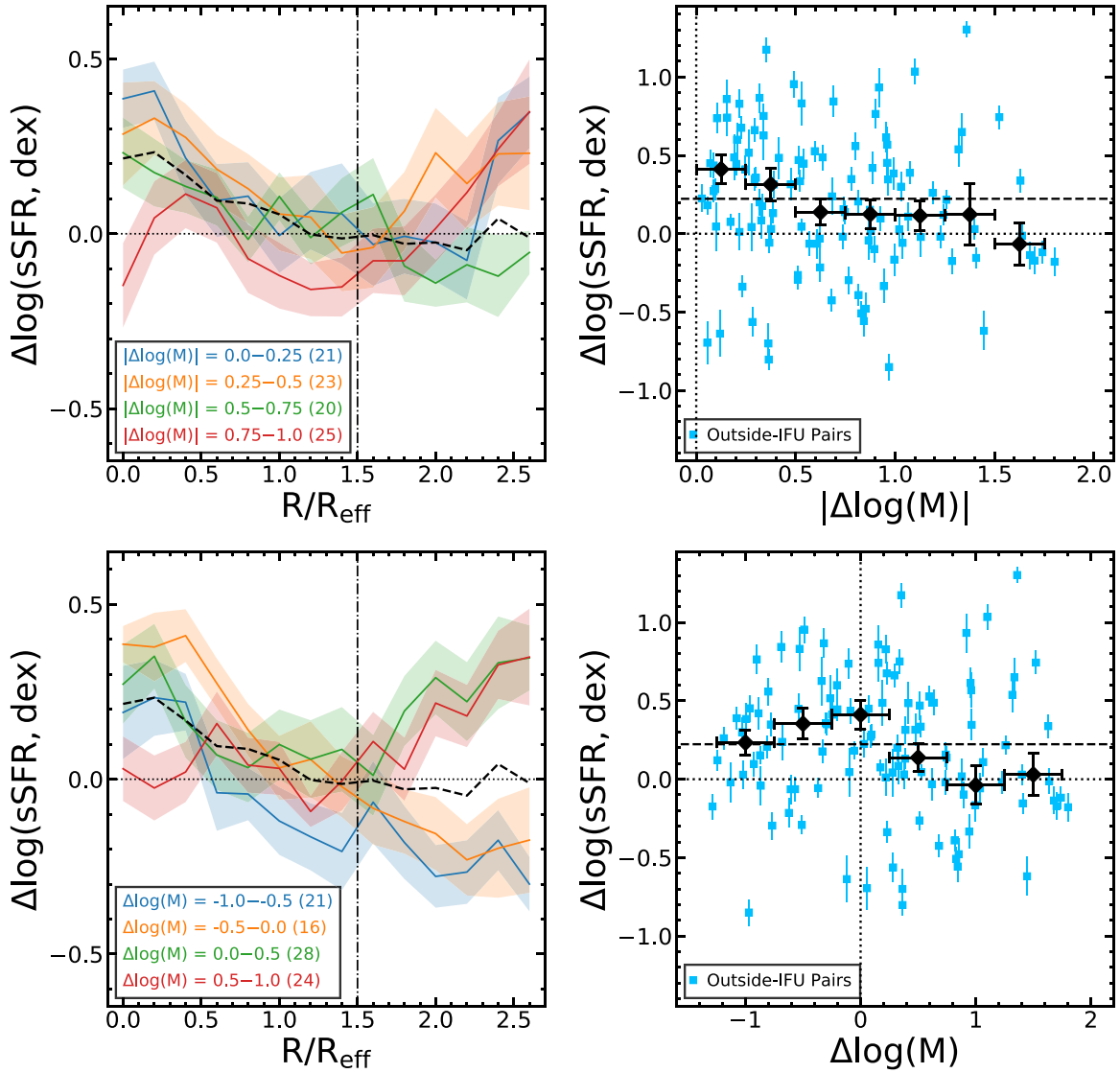


Figure 6. Same as Figure 4 except the difference profiles are split by the mass ratio of the pair. The top row is the absolute value of the mass ratio, and the bottom row is the mass ratio without taking the absolute value. Taking the mass ratio without the absolute value allows us to separately study the more-massive companions of pairs and the less-massive companions of pairs. The inside-IFU sample is left out of this analysis because we do not yet have reliable measurements of their total stellar-mass ratios.

enhanced by 0.2 dex, while at $\Delta\log(M) = 1.0$, the sSFR enhancement is zero.

We also see that the $\Delta\log(\text{sSFR})$ values in the outskirts ($R > 1.5 R_{\text{eff}}$) of the pairs have a dependence on the mass ratio in the bottom right of Figure 6. Primary companions show a positive enhancement of 0.0–0.4 dex to the sSFR in their outskirts, while secondary companions feature a suppression of the sSFR in their outskirts of about 0.0–0.3 dex. Again we note that only 37% of the MaNGA sample is designed to extend beyond $1.5 R_{\text{eff}}$; however, a similar result has been observed in the hydrodynamical simulations of Moreno et al. (2015) and Moreno et al. (2020).

From the mass ratio, we see two different effects. First, we see that the central enhancement of the sSFR is strongest for pairs with 1:1 mass ratios. Second, we see that secondary companions show steeper enhancement profiles with higher levels of sSFR enhancement in their centers and stronger levels of sSFR suppression in their disks with respect to primary companions. Finally, we see that primary companions feature

sSFR enhancement at wide radii, while secondary companions feature sSFR suppression at wide radii.

4.3. Dependence on Projected Separation

A number of previous studies have shown that the sSFR enhancement increases as projected separation decreases (e.g., Li et al. 2008; Ellison et al. 2008; Scudder et al. 2012; Patton et al. 2013), in agreement with simulations (Scudder et al. 2012).

Figure 7 shows the profile and the central level of sSFR enhancement as a function of the projected separation (r_p) from our MaNGA data. The $\Delta\log(\text{sSFR})$ profiles show only a weak dependency on the projected separation. The pairs below a separation of 25 kpc have $\Delta\log(\text{sSFR})$ profiles that lie ~ 0.1 dex above the sample median, while the profiles of the pairs beyond 25 kpc are ~ 0.1 dex below the sample median.

A dependence on the projected separation can be seen more clearly when looking at the data extracted from the inner $0.5 R_{\text{eff}}$. The level of the enhancement gradually increases with

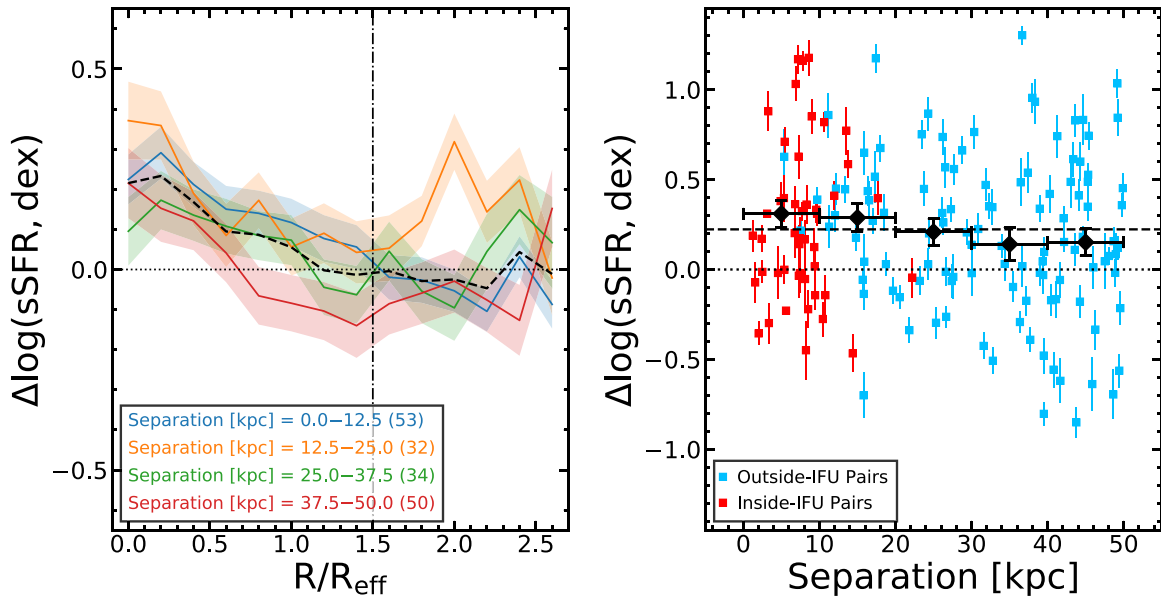


Figure 7. Same as Figure 4 except the difference profiles are split by projected separation.

closer separation from 50 kpc to 10 kpc. While $\Delta\log(\text{sSFR})$ falls at higher separations, there is still a substantial level of enhancement between 40 and 50 kpc of ~ 0.15 dex. Within 10 kpc, the $\Delta\log(\text{sSFR})$ enhancement jumps to ~ 0.3 dex. Our data show that the sSFR enhancement persists out to at least $r_p = 50$ kpc, which is the limit of our pair selection.

5. Discussion

5.1. Radial Profiles of Enhancement

In Figure 8 we compare the $\Delta\log(\text{sSFR})$ profile and $\Delta\log(\text{SFR})$ as a function of galactocentric radius between our work and previous works using the MaNGA data. Thorp et al. (2019) studied a sample of 36 postmergers from the MaNGA sample. The centers of the postmerger galaxies feature a greater level of sSFR enhancement in their centers than our galaxy pairs of $\Delta\log(\text{SFR}) = 0.40\text{--}0.45$, roughly 0.2 dex higher than our paired galaxies. In the range $0.4\text{--}1.0 R_{\text{eff}}$, the postmerger galaxies and our pairs are in closer agreement, being 0.05–0.1 dex higher than our paired galaxies. Beyond $1.0 R_{\text{eff}}$, the postmerger galaxies have a higher $\Delta\log(\text{SFR})$ by about 0.1–0.2 dex. The heightened level of sSFR enhancement in the centers of postmerger galaxies in comparison to merging galaxies seems consistent with the idea that a second and greater burst of star formation occurs as the two merging galaxies coalesce into a single galaxy.

Pan et al. (2019) studied a set of 205 paired galaxies in the MaNGA sample, focusing on the sSFR enhancement as a function of the merger interaction stage. The $\Delta\log(\text{sSFR})$ profiles of the galaxy pairs in Pan et al. (2019) are $\sim 0.10\text{--}0.15$ dex above the profiles in our sample. Our paired galaxies show a slight sSFR suppression in their disks past $1.0 R_{\text{eff}}$, while the galaxy pairs in Pan et al. (2019) show an enhancement of ~ 0.15 dex to the sSFR in their disks.

The reason for the discrepancies between our samples may be that Pan et al. (2019) includes a set of 96 pairs that are too close to be separately deblended by SDSS and instead were visually identified by their morphology. Eighty-two of these pairs are postmerger galaxies. Pan et al. (2019) showed that pairs with a disturbed morphology have higher $\Delta\log(\text{SFR})$ than pairs without morphological distortions. Further, Thorp et al. (2019) showed

that postmerger galaxies have $\Delta\log(\text{SFR})$ profiles that are elevated over our sample’s profiles. From this, we infer that the lower $\Delta\log(\text{sSFR})$ seen in our sample is due to our sample’s lack of postmerger galaxies.

5.2. Central Enhancement versus Merger Parameters

While in this work we find that $\Delta\log(\text{sSFR})$ has essentially no dependence on the stellar mass of the galaxy, Li et al. (2008) found that lower mass galaxies experience greater levels of enhancement than higher mass galaxies. Galaxies in the mass range $\log(M/M_\odot) \geq 9.72$ were shown to experience an enhancement ~ 0.4 dex higher than galaxies in the mass range $\log(M/M_\odot) \geq 10.6$.

The source of the difference is unclear; between our works we utilize different methods for determining the sSFR enhancement in galaxy pairs. Li et al. (2008) defines their enhancement function as the average sSFR of the paired galaxies at a given separation, weighted by the number of companions, subtracted by the average sSFR of the whole sample. While we do not find the same dependency between the sSFR enhancement and stellar mass, the sSFR enhancement as a function of projected separation between our studies is in good agreement (see Figure 9).

The dependence of the SFR enhancement on the mass ratio was studied in Ellison et al. (2008). They found that pairs with mass ratios of 2:1 have higher SFR enhancements of ~ 0.1 dex over pairs with wider 10:1 mass ratios. We find that pairs with mass ratios of $\Delta\log(M) = 0.25$ (1.8:1) are 0.2 dex over pairs with mass ratios of $\Delta\log(M) = 1.0$ (10:1). Ellison et al. (2008) also saw tentative evidence for SFR enhancement in the secondary companions of minor pairs. We not only confirm that secondary companions of minor pairs feature SFR enhancement, but also that the enhancement is higher than the primary component of pairs at the same mass ratios.

The observations are also consistent with simulations. Moreno et al. (2015) used GADGET-3, a smoothed particle hydrodynamics code, to study the spatial extent of the star formation enhancement. The merger simulations showed that the star formation enhancement was largely concentrated in the

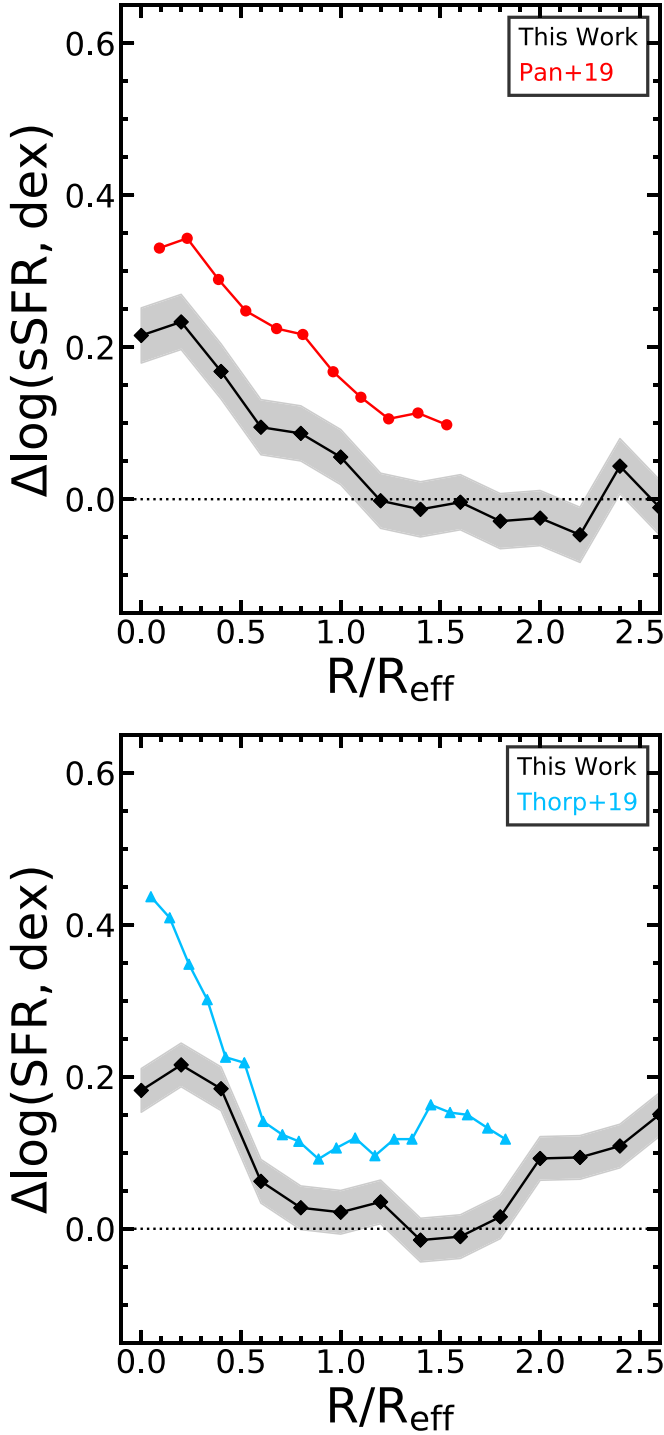


Figure 8. Mean radial profile of $\Delta\log(\text{sSFR})$ (top) and $\Delta\log(\text{SFR})$ (bottom) between pairs and controls of this work with the tailored-control method (black) compared against those of Pan et al. (2019; red), a pair sample, and Thorp et al. (2019; blue), a postmerger sample.

centers ($R < 1$ kpc) of the paired galaxies and that the off-nuclear regions ($1 < R < 10$ kpc) showed a suppression of star formation. Moreno et al. (2015) also found that lower mass secondary galaxies (in mergers with stellar mass ratios of 2.5:1) have higher levels of sSFR enhancement in their centers and have stronger levels of sSFR suppression in their disks. This is in good agreement with our work: we found that secondary companions show moderately higher levels of sSFR enhancement in their centers in comparison to primary companions at

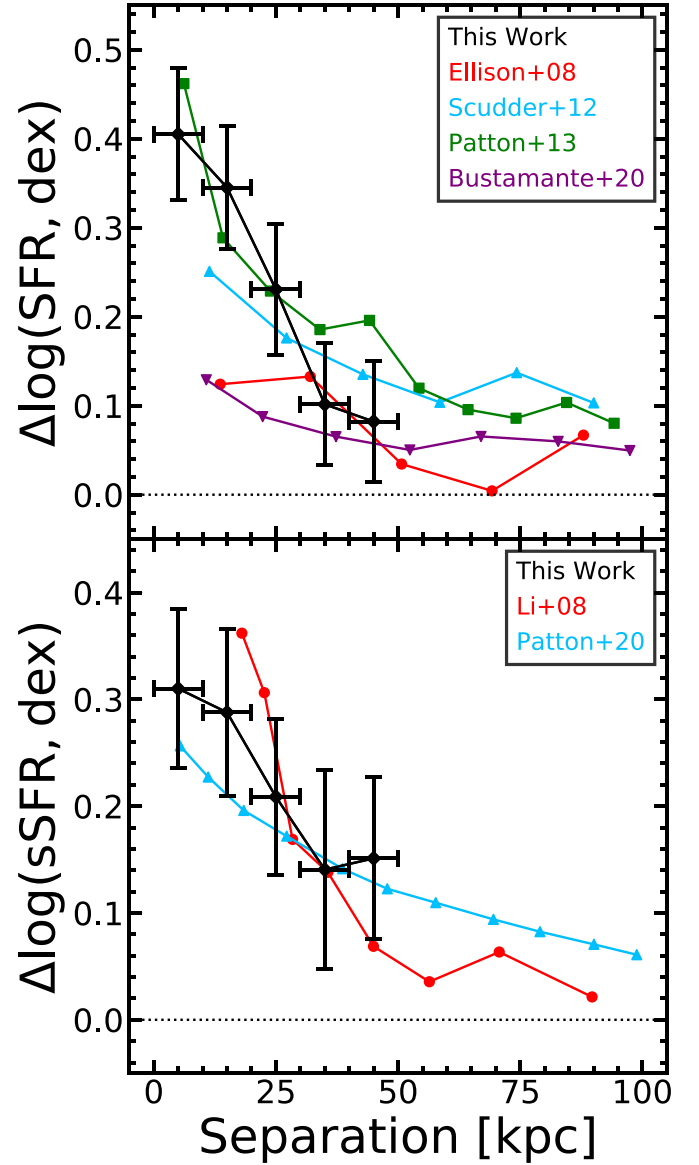


Figure 9. Top: $\Delta\log(\text{SFR})$ extracted from the inner $0.5 R_{\text{eff}}$ over the projected separation from this study (black), Ellison et al. (2008; red), Scudder et al. (2012; blue), Patton et al. (2013; green), and Bustamante et al. (2020; purple). Bottom: $\Delta\log(\text{sSFR})$ extracted from the inner $0.5 R_{\text{eff}}$ over the projected separation from this study (black), Li et al. (2008; red), and Patton et al. (2020; blue).

the same mass ratio. Further, the outskirts of our primary companions feature positive enhancement to their sSFR, while the secondary companions show a strong suppression of the sSFR in their outskirts.

Figure 9 compares the enhancement in both SFR and sSFR as a function of projected separation. For our data points, we use the mean $\Delta\log\text{SFR}$ and $\Delta\log\text{sSFR}$ measured within a deprojected radius of $0.5 R_{\text{eff}}$ (i.e., the black data points in the right panel of Figure 7). The literature data are measured from single $1''$ – $1.5''$ -radius SDSS fibers (Ellison et al. 2008; Scudder et al. 2012; Patton et al. 2013; Bustamante et al. 2020). We find that our central SFR enhancements for closely separated pairs are higher than many of the previous studies: our sSFR enhancement is ~ 0.1 dex higher than in Scudder et al. (2012) and ~ 0.2 dex higher than in Ellison et al. (2008) and Bustamante et al. (2020). The central enhancement to the sSFR for closely

separated pairs in our sample is ~ 0.05 dex lower than in Patton et al. (2013). The sSFR enhancement function from Li et al. (2008) is 0.05–0.10 dex above our sample at close separations.

The sSFR as a function of separation was studied with the cosmological hydrodynamical simulations of IllustrisTNG (Patton et al. 2020). In Figure 9 we show the $\Delta\log(\text{sSFR})$ enhancements across 2D separation (projected separation) from the TNG300-1 simulation. Patton et al. (2020) found an sSFR enhancement that is $1.8\times$ that of the isolated controls within a separation of 15 kpc and is statistically significant out to a 2D separation of ~ 250 kpc. This enhancement is ~ 0.05 dex lower than ours; however, our sSFR enhancement shown in Figure 9 was extracted from a $0.5 R_{\text{eff}}$ aperture, while Patton et al. (2020) extracted the sSFR from a 50% half-mass radius. This means that our extraction radius is effectively twice as small and is more restricted to the central burst of star formation.

Our sample only covers projected separations within 50 kpc, while previous surveys cover out to 100–200 kpc. While our sample covers a smaller separation range, the $\Delta\log(\text{SFR})$ of our sample at 50 kpc is roughly the same level as that of Ellison et al. (2008) and Bustamante et al. (2020) at the same projected separation. From this we see that our sSFR enhancement as a function of projected separation is consistent with what has been found in previous works.

5.3. Comparison with Simulations

Our results are consistent with the idea that galaxy merger events trigger a burst of star formation in the centers of the paired galaxies. In this model, when two galaxy pairs undergo their first pericenter, the tidal torques exerted on the disks of interacting galaxies form barred structures. These barred structures funnel gases into the centers of the galaxies, a process that triggers a burst of new star formation. Eventually, as the pairs separate from each other after the first pericenter, the burst of star formation begins to subside. This is shown in our work and many previous works in Figure 9, where the sSFR enhancement is greatest for close separations and falls with wider separations. We also found that the $\Delta\log(\text{sSFR})$ is independent of the stellar mass. This means that the merger event will produce the same amount of new stellar mass for low-mass galaxies as it produces for high-mass galaxies. This also means that the low-mass galaxies will experience a greater change in total stellar mass before and after the merger event, so the merger event will have a greater impact on the mass evolution of low-mass galaxies as opposed to high-mass galaxies.

We find that the strength of the central burst of merger-induced star formation is dependent on the relative masses between the two galaxies. Equal-mass galaxies see the strongest bursts of star formation, while wide mass ratios see weaker bursts of star formation. We further find that the strength of the central burst of star formation differs between the primary and secondary companion of a pair, where the less-massive secondary companion features a higher level of sSFR enhancement in comparison to its higher mass primary companion.

Moreno et al. (2020) use galaxy merger simulations to study the origin of the enhanced star formation in galaxy pairs, whether it is an increase in the star formation efficiency, defined as the ratio between the SFR and the mass of cold dense gas, or it is an increase in the availability of cold dense gas. They find that the star formation in secondary galaxies is

evenly split between being efficiency-driven or fuel-driven systems, while primary galaxies are more likely to be fuel-driven systems (71%). Moreno et al. (2020) also find that secondary galaxies feature higher levels of star formation enhancement than primary galaxies do, which is in agreement with what we find in this work. This indicates that the reason that primary galaxies behave differently from secondary galaxies may be a difference in the physical mechanism that drives the enhanced star formation.

We also find that there is a difference in the $\Delta\log(\text{sSFR})$ offsets at wide radii between primary and secondary companions. The primary companion features an enhancement to its sSFR at wide radii, while the secondary companion features a suppression to its sSFR at wide radii. The reason for this is unclear; however, this means that the primary companions will experience enhanced stellar-mass growth across their disks, while the secondary companions will only see substantial stellar-mass growth in their centers, which will result in more bulge-dominated galaxies. Differences in the bulge-to-total ratio, (B/T), have been observed in previous works like Bluck et al. (2019), who found that satellites tend to have slightly higher (B/T) than central galaxies at the same stellar mass.

6. Summary and Conclusion

In this paper, we have demonstrated the power of a massive integral-field spectroscopic survey in comparison studies of galaxy properties. The nearby galaxy populations show consistent behaviors despite their large diversity in star formation properties. Stacking was able to detect the signal buried in the noise by averaging, in the time domain, the likely stochastic star-forming histories of galaxies (which drive the scatter in the sample). We focused on comparing the azimuthally averaged radial profiles of sSFR between galaxies in close pairs and a control sample of isolated galaxies. In agreement with previous studies, we found that, on average, star formation is elevated in close galaxy pairs. The properties of these purported merger-induced differences in sSFR can be summarized as follows:

1. Star formation is enhanced within the inner $1.0 R_{\text{eff}}$ and it peaks at a level of $0.20\text{--}0.25 \pm 0.1$ dex (i.e., about two times faster star formation). On the other hand, the outskirts of the paired galaxies ($R_{\text{eff}} = 1.0\text{--}2.5$) show a moderate amount of suppression in sSFR at a level of ~ 0.1 dex.
2. The sSFR difference profile is largely independent of the stellar mass.
3. The level of central sSFR enhancement increases at smaller projected separations.
4. The level of central sSFR enhancement depends on the mass ratio of the galaxy pair. Galaxies with small mass ratios, $|\Delta\log(M)| = 0.0\text{--}0.5$, see an enhancement $\sim 0.1\text{--}0.2$ dex higher than the average. But the enhancement is still present in pairs with mass ratios as large as $|\Delta\log(M)| = 1.0$.
5. The merger-induced changes in sSFR also seem to differ between the more-massive and the less-massive member of a galaxy pair. At the same mass ratio, the less-massive member in a galaxy pair shows a higher sSFR enhancement (by $\sim 0.1\text{--}0.2$ dex) than the more-massive member does.
6. At large radii ($R/R_{\text{eff}} > 1.5$), the more-massive companions in pairs show an enhancement to the sSFR, while


the less-massive companions in pairs show a suppression to the sSFR.

As of 2020 August 24, MaNGA has completed its observations of $\sim 10,000$ galaxies. This final sample gives us access to an unprecedentedly large sample of paired and control galaxies with $2''$ spatial sampling up to $2-3 R_{\text{eff}}$, which will undoubtedly improve the results presented here. In addition, the less-massive members of the inside-IFU pairs can be included in such a comparison study once we build a better deblended photometric catalog using SDSS images.

We thank the anonymous referee for the useful comments and suggestions. We also thank Cheng Li for our useful discussion on how the sSFR enhancement in galaxy pairs relates to their stellar mass and mass ratio. J.S. and H.F. acknowledge support from the National Science Foundation (NSF) grant AST-1614326. Y.S.D. would like to acknowledge support from NSFC grant No. 10878003. Funding for the Sloan Digital Sky Survey IV has been provided by the Alfred P. Sloan Foundation, the U.S. Department of Energy Office of Science, and the Participating Institutions. SDSS acknowledges support and resources from the Center for High-Performance Computing at the University of Utah. The SDSS website is www.sdss.org.

SDSS is managed by the Astrophysical Research Consortium for the Participating Institutions of the SDSS Collaboration, including the Brazilian Participation Group, the Carnegie Institution for Science, Carnegie Mellon University, the Chilean Participation Group, the French Participation Group, Harvard-Smithsonian Center for Astrophysics, Instituto de Astrofísica de Canarias, The Johns Hopkins University, Kavli Institute for the Physics and Mathematics of the Universe (IPMU)/University of Tokyo, the Korean Participation Group, Lawrence Berkeley National Laboratory, Leibniz Institut für Astrophysik Potsdam (AIP), Max-Planck-Institut für Astronomie (MPIA Heidelberg), Max-Planck-Institut für Astrophysik (MPA Garching), Max-Planck-Institut für Extraterrestrische Physik (MPE), National Astronomical Observatories of China, New Mexico State University, New York University, University of Notre Dame, Observatório Nacional/MCTI, The Ohio State University, Pennsylvania State University, Shanghai Astronomical Observatory, United Kingdom Participation Group, Universidad Nacional Autónoma de México, University of Arizona, University of Colorado Boulder, University of Oxford, University of Portsmouth, University of Utah, University of Virginia, University of Washington, University of Wisconsin, Vanderbilt University, and Yale University.

ORCID iDs

Joshua L. Steffen  <https://orcid.org/0000-0003-3299-9595>
 Hai Fu  <https://orcid.org/0000-0001-9608-6395>
 Y. Sophia Dai (戴昱)  <https://orcid.org/0000-0002-7928-416X>
 Shuai Feng  <https://orcid.org/0000-0002-9767-9237>
 Arran C. Gross  <https://orcid.org/0000-0001-7681-9213>
 Rui Xue  <https://orcid.org/0000-0001-7689-9305>

References

- Abolfathi, B., Aguado, D. S., Aguilar, G., et al. 2018, *ApJS*, **235**, 42
 Baldwin, J. A., Phillips, M. M., & Terlevich, R. 1981, *PASP*, **93**, 5
 Barnes, J. E., & Hernquist, L. 1996, *ApJ*, **471**, 115
 Barnes, J. E., & Hernquist, L. E. 1991, *ApJL*, **370**, L65
 Barrera-Ballesteros, J. K., Sánchez, S. F., García-Lorenzo, B., et al. 2015, *A&A*, **579**, A45
 Belfiore, F., Maiolino, R., Bundy, K., et al. 2018, *MNRAS*, **477**, 3014
 Belfiore, F., Westfall, K. B., Schaefer, A., et al. 2019, *AJ*, **158**, 160
 Bluck, A. F. L., Bottrell, C., Teimoorinia, H., et al. 2019, *MNRAS*, **485**, 666
 Bundy, K., Bershady, M. A., Law, D. R., et al. 2015, *ApJ*, **798**, 7
 Bustamante, S., Ellison, S. L., Patton, D. R., & Sparre, M. 2020, *MNRAS*, **494**, 3469
 Capelo, P. R., Dotti, M., Volonteri, M., et al. 2017, *MNRAS*, **469**, 4437
 Cappellari, M. 2017, *MNRAS*, **466**, 798
 Cardelli, J. A., Clayton, G. C., & Mathis, J. S. 1989, *ApJ*, **345**, 245
 Cid Fernandes, R., Stasińska, G., Mateus, A., & Vale Asari, N. 2011, *MNRAS*, **413**, 1687
 Cooray, A., & Sheth, R. 2002, *PhR*, **372**, 1
 Drory, N., MacDonald, N., Bershady, M. A., et al. 2015, *AJ*, **149**, 77
 Ellison, S. L., Patton, D. R., Simard, L., & McConnachie, A. W. 2008, *AJ*, **135**, 1877
 Fu, H., Steffen, J. L., Gross, A. C., et al. 2018, *ApJ*, **856**, 93
 Giovanelli, R., Haynes, M. P., Salzer, J. J., et al. 1994, *AJ*, **107**, 2036
 Kewley, L. J., Dopita, M. A., Sutherland, R. S., Heisler, C. A., & Trevena, J. 2001, *ApJ*, **556**, 121
 Lacerda, E. A. D., Sánchez, S. F., Cid Fernandes, R., et al. 2020, *MNRAS*, **492**, 3073
 Larson, R. B., & Tinsley, B. M. 1978, *ApJ*, **219**, 46
 Law, D. R., Yan, R., Bershady, M. A., et al. 2015, *AJ*, **150**, 19
 Lawson, C. L., & Hanson, R. J. 1974, Solving least squares problems (Prentice-Hall Series in Automatic Computation) (Englewood Cliffs, NJ: Prentice-Hall)
 Li, C., Kauffmann, G., Heckman, T. M., Jing, Y. P., & White, S. D. M. 2008, *MNRAS*, **385**, 1903
 Markwardt, C. B. 2009, in ASP Conf. Ser., Astronomical Data Analysis Software and Systems XVIII, ed. D. A. Bohlender, D. Durand, & P. Dowler (San Francisco, CA: ASP), **251**
 Mihos, J. C., & Hernquist, L. 1996, *ApJ*, **464**, 641
 Moreno, J., Torrey, P., Ellison, S. L., et al. 2015, *MNRAS*, **448**, 1107
 Moreno, J., Torrey, P., Ellison, S. L., et al. 2020, *MNRAS*
 Murphy, E. J., Condon, J. J., Schinnerer, E., et al. 2011, *ApJ*, **737**, 67
 Noeske, K. G., Weiner, B. J., Faber, S. M., et al. 2007, *ApJL*, **660**, L43
 O'Donnell, J. E. 1994, *ApJ*, **422**, 158
 Pan, H.-A., Lin, L., Hsieh, B.-C., et al. 2019, *ApJ*, **881**, 119
 Patton, D. R., Torrey, P., Ellison, S. L., Mendel, J. T., & Scudder, J. M. 2013, *MNRAS*, **433**, L59
 Patton, D. R., Wilson, K. D., Metrow, C. J., et al. 2020, *MNRAS*, **494**, 4969
 Perez, J., Michel-Dansac, L., & Tissera, P. B. 2011, *MNRAS*, **417**, 580
 Pillepich, A., Nelson, D., Hernquist, L., et al. 2018, *MNRAS*, **475**, 648
 Rodriguez-Gomez, V., Pillepich, A., Sales, L. V., et al. 2016, *MNRAS*, **458**, 2371
 Rupke, D. S. N., Kewley, L. J., & Chien, L. H. 2010, *ApJ*, **723**, 1255
 Sánchez, S. F., Avila-Reese, V., Hernandez-Toledo, H., et al. 2018, *RMxAA*, **54**, 217
 Sánchez, S. F., Pérez, E., Sánchez-Blázquez, P., et al. 2016a, *RMxAA*, **52**, 21
 Sánchez, S. F., Pérez, E., Sánchez-Blázquez, P., et al. 2016b, *RMxAA*, **52**, 171
 Scudder, J. M., Ellison, S. L., Torrey, P., Patton, D. R., & Mendel, J. T. 2012, *MNRAS*, **426**, 549
 Simard, L., Mendel, J. T., Patton, D. R., Ellison, S. L., & McConnachie, A. W. 2011, *ApJS*, **196**, 11
 Thorp, M. D., Ellison, S. L., Simard, L., Sánchez, S. F., & Antonio, B. 2019, *MNRAS*, **482**, L55
 Toomre, A., & Toomre, J. 1972, *ApJ*, **178**, 623
 van der Marel, R. P., & Franx, M. 1993, *ApJ*, **407**, 525
 Vazdekis, A., Ricciardelli, E., Cenarro, A. J., et al. 2012, *MNRAS*, **424**, 157
 Wake, D. A., Bundy, K., Diamond-Stanic, A. M., et al. 2017, *AJ*, **154**, 86
 Zehavi, I., Blanton, M. R., Frieman, J. A., et al. 2002, *ApJ*, **571**, 172